

Physics-Informed Neural Network for Solving the Diffusion Equation in the Expanding QCD Medium

Wenhua Fan,¹ Jiamin Liu,² Huansang Yang,³ and Baoyi Chen^{1, 2, *}

¹*The International Joint Institute of Tianjin University,
Fuzhou, Tianjin University, Tianjin 300072, China*

²*Department of Physics, School of Science, Tianjin University, Tianjin 300354, China*

³*College of Engineering, Georgia Institute of Technology, Atlanta, GA 30332, United States*

(Dated: January 13, 2026)

We employ Physics-Informed Neural Networks (PINNs) to solve the diffusion of heavy quarks within the expanding hot QCD medium generated in relativistic heavy-ion collisions. Due to the strong coupling between heavy quarks and the bulk medium, the evolution of heavy quarks can be effectively characterized by a diffusion equation. This approach assumes the instantaneous kinetic thermalization of heavy quarks following their production in nuclear collisions. The local density of heavy quarks is intrinsically coupled to the velocity profile of the hot QCD medium. By incorporating the fluid velocity profiles provided by a hydrodynamic model directly into the diffusion equation, we utilize the deep neural network (DNN) to efficiently determine the heavy-quark evolution. Furthermore, this work provides a valuable reference for the application of deep learning techniques to the treatment of non-thermalized heavy-quark dynamics. The rapid calculation of heavy-quark diffusion using DNNs further facilitates the study of heavy-quark coalescence within a large ensemble of fluctuating hot media.

I. INTRODUCTION

Relativistic heavy-ion collisions produce a strongly coupled, deconfined medium known as the quark-gluon plasma (QGP) [1]. Over the past several decades, experiments at the Relativistic Heavy Ion Collider (RHIC) and the Large Hadron Collider (LHC) have measured the production and momentum distributions of various hadrons to characterize the properties of strong interactions at extreme temperatures [2, 3]. Extensive studies interpreting these data indicate that the deconfined medium behaves as a nearly perfect fluid [4–6]. Heavy quarks, produced via hard parton scatterings at the onset of nuclear collisions, serve as sensitive probes of this early-stage medium, which typically possesses a lifetime on the order of a few fm/c [7–9]. The dynamical evolution of heavy quarks is commonly described by the Langevin equation [10, 11] or the Boltzmann-type transport equation [12]. Due to their strong coupling with the bulk medium, heavy quarks undergo significant energy loss in Pb-Pb collisions at LHC energies. In collisions where multiple charm-quark pairs are produced, charm and anti-charm quarks may recombine within the deconfined medium, hadronizing into bound-state heavy quarkonia. This process, known as regeneration or coalescence, can significantly enhance the charmonium yield—a phenomenon well-established by experimental observations [13–16]. Because the charmonium yield from coalescence is highly sensitive to the phase-space density of charm quarks [17, 18], accurately determining this density within the expanding hot QCD medium is essential for a quantitative understanding of both open and hidden

heavy-flavor production.

In the strong coupling limit, heavy quarks produced in parton hard scattering are assumed to immediately reach kinetic thermalization in the hot QCD medium. The dynamics of charm quarks can be effectively approximated with the diffusion equation. The spatial density of charm quarks is governed by the flow velocities of the expanding medium. However, in event-by-event nuclear collisions, the fluid velocity profiles fluctuate, indicating that the charm diffusion process differs in each collision event [19]. Numerically solving the charm diffusion in an event-by-event fluctuating bulk medium is crucial but computationally expensive, requiring significant computational resources.

The Physics-Informed Neural Network (PINN) framework was first introduced by Raissi et al. [20]. PINNs transform the task of solving partial differential equations (PDEs) into an optimization problem by minimizing a loss function. This loss function is defined by the residuals of the governing PDEs, alongside the initial and boundary conditions evaluated at collocation points, sampled randomly or systematically, within the physical domain [21]. Consequently, the underlying physical laws are encoded directly into the neural network’s training process through this loss formulation.

Compared with traditional numerical methods, Physics-Informed Neural Networks (PINNs) utilize automatic differentiation to compute derivatives efficiently. This approach eliminates the need for manual derivation and mitigates numerical errors typically associated with discretization in conventional solvers—a feature that is particularly advantageous for high-dimensional problems. Because PINNs are mesh-free, they can effectively solve PDEs involving complex geometries or irregular boundaries without the computational overhead of mesh generation. Another significant advantage of the

* baoyi.chen@tju.edu.cn

PINN framework is its capacity for multiscale modeling, enabling it to capture both microscopic and macroscopic physical behaviors simultaneously. Furthermore, several studies have investigated the dynamics of the PINN training process, employing the Neural Tangent Kernel (NTK) framework to stabilize of PINNs [22].

PINNs have been further extended to solve stochastic differential equations [23, 24] and to simulate computational fluid dynamics within complex geometries [25–27]. In this work, we employ the PINN framework to investigate the evolution of charm-quark densities within the expanding QCD medium generated in relativistic nuclear collisions. This approach enables the determination of charm-quark evolution in an arbitrary fluctuating medium, facilitating comprehensive charmonium production calculations with an event-by-event fluctuations [28]. Such an advancement is critical for understanding experimental data regarding charmonium anisotropic flow [29].

The remainder of this paper is organized as follows. We first utilize a hydrodynamic model to simulate the evolution of the bulk medium. This fluid information is then incorporated into the charm-quark diffusion equation. Finally, we introduce the PINN model designed to solve the diffusion equation within the context of an expanding medium.

II. CHARM DIFFUSION EQUATION AND HOT MEDIUM

The dynamical evolution of the strongly coupled, deconfined medium produced in relativistic heavy-ion collisions has been extensively investigated using hydrodynamic models [30]. In this work, we utilize the MUSIC package [31, 32] to simulate the temperature and velocity profiles of the fluid in Pb-Pb collisions at $\sqrt{s_{NN}} = 5.02$ TeV. The equation of state (EoS) for the deconfined phase is derived from lattice QCD calculations, whereas the EoS for the hadronic phase is based on the Hadron Resonance Gas model [33, 34]. The transition between the confined and deconfined phases is modeled as a smooth crossover. Furthermore, the initial energy density of the medium is determined via the Glauber model, with additional constraints provided by the final-state charged-particle multiplicity.

Heavy quarks are produced during the early stages of the collision. Due to their large masses, thermal production in the hot QCD medium is negligible, and the total number of charm quarks is conserved during the medium's expansion. Lattice QCD calculations suggest a very strong coupling between heavy quarks and the hot QCD medium [35, 36]. Assuming kinetic thermalization, the momentum distribution of charm quarks follows the normalized Fermi-Dirac distribution, while the local density $\rho_c(\tau, \mathbf{r})$ is governed by the conservation equation [37]:

$$\partial_\mu(\rho_c u^\mu) = 0, \quad (1)$$

Flow Velocity Field at different time

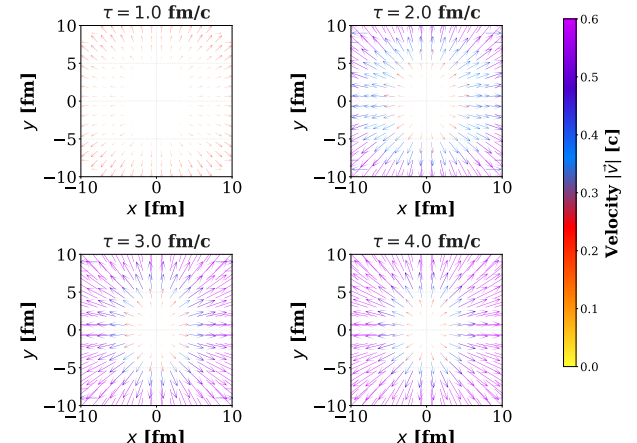


FIG. 1: The fluid velocity distributions at the central rapidity region for Pb-Pb collisions at $\sqrt{s_{NN}} = 5.02$ TeV generated by MUSIC package, with an impact parameter of $b = 6$ fm, are presented. The direction and color of the arrows represent the local velocity vectors and their corresponding magnitudes, respectively. The four panels illustrate the temporal evolution of the velocity distribution at distinct proper time points.

where $u^\mu = \gamma(1, \mathbf{v})$ is the fluid four-velocity, γ is the Lorentz factor, and \mathbf{v} is the three-dimensional fluid velocity. In Pb-Pb collisions, the longitudinal expansion of the medium is effectively described by the Bjorken model. Under the assumption of full kinetic thermalization, the charm-quark density can be factorized as $\rho_c(\tau, \mathbf{x}_T, \eta) = \rho_T(\tau, \mathbf{x}_T) \rho_\eta(\eta) \cosh \eta/\tau$, where ρ_T is the density in the transverse plane and η is the spacetime pseudo-rapidity. The function $\rho_\eta(\eta)$ represents the normalized longitudinal distribution of charm quarks, which is often approximated as unity in the mid-rapidity region. Here, $\tau = \sqrt{t^2 - z^2}$ denotes the proper time. The longitudinal Bjorken expansion reduces the charm-quark density by a factor of $1/\tau$. In the central rapidity region, the conservation equation simplifies to:

$$\frac{\partial \rho_T(\tau, x, y)}{\partial \tau} = -\frac{\partial(\rho_T v_x)}{\partial x} - \frac{\partial(\rho_T v_y)}{\partial y} \quad (2)$$

where $v_x(\tau, x, y)$ and $v_y(\tau, x, y)$ represent the local transverse velocities of the medium, as provided by the hydrodynamic model. The local density of charm quarks is highly sensitive to these fluid velocity profiles. In event-by-event collisions, the presence of fluctuations causes the fluid velocities to vary significantly across different events, necessitating an individual solution to the diffusion equation for each collision event. While several numerical methods, such as the finite element and finite difference methods, are available to solve this equation, they often suffer from substantial computational costs

or introduce significant numerical uncertainties due to discretization. Physics-Informed Neural Networks can be employed to solve the partial differential equation, even when the coefficients of PDE (such as the velocity fields $v_{x,y}(\tau, x, y)$) exhibit high complexity. By passing the grid-based constraints of traditional numerical methods and the data-intensive requirements of purely data-driven models, this approach provides a robust and efficient framework for solving both forward and inverse problems in heavy-quark dynamics.

Regarding the initial spatial density of charm quarks, since they are produced via binary nucleon-nucleon collisions, their density is proportional to the product of the nuclear thickness functions:

$$\rho_T(\tau = 0, \mathbf{x}_T) = \sigma_{NN}^{c\bar{c}} T_A(\mathbf{x}_T - \mathbf{b}/2) T_B(\mathbf{x}_T + \mathbf{b}/2), \quad (3)$$

where $\sigma_{NN}^{c\bar{c}}$ represents the charm-pair production cross section within a specified rapidity interval. In this work, as we focus on the longitudinal and transverse diffusion of charm quarks while assuming total number conservation, this cross section is taken as unity to determine the relative charm-quark density within the expanding medium. The thickness functions $T_{A,B}$ for the lead (Pb) nuclei are calculated assuming a nucleon density that follows a Woods-Saxon distribution. The impact parameter \mathbf{b} denotes the transverse distance between the centers of the two nuclei at the moment of impact. The hydrodynamic evolution of the medium, simulated for Pb-Pb collisions at $\sqrt{s_{NN}} = 5.02$ TeV, begins at an initial proper time of $\tau_0 = 0.6$ fm/c. We assume that for $\tau < \tau_0$, the charm quarks undergo primarily longitudinal expansion. Consequently, the diffusion evolution governed by Eq. (2) is initialized at τ_0 , with the initial spatial profile given by $\rho_T(\tau_0, \mathbf{x}_T) = \rho_T(0, \mathbf{x}_T)$.

III. DEEP NEURAL NETWORK

The foundational principle of PINNs is the integration of mathematical models, typically expressed as PDEs along with their corresponding initial and boundary conditions, directly into the neural network's loss function as prior physical knowledge. By embedding these governing equations, PINNs significantly reduce the dependency on large, high-resolution labeled datasets. Consequently, training a PINN is formulated as an optimization problem: the objective is to identify an optimal set of network parameters that minimizes the composite loss function. This process yields a continuous solution that satisfies both the underlying physical laws and the specific constraints of the problem.

The input to the PINN consists of the coordinates (τ, x, y) , while the output is the charm quark density $\rho_{nn}(\tau, x, y; \theta)$, where θ denotes the trainable parameters (weights and biases) of the network. Typically structured as a multilayer perceptron, the network provides an implicit solution representation that is continuous and in-

finitely differentiable throughout the computational domain. The parameters θ are iteratively updated to minimize a composite loss function, ensuring the solution adheres to both the constraints and the governing physical laws.

The loss function is defined as a weighted sum of the PDE residual loss \mathcal{L}_{PDE} , the initial condition loss \mathcal{L}_{IC} , and the boundary condition loss \mathcal{L}_{BC} . These components quantify the discrepancy between the network's prediction, $\rho_{nn}(\tau, x, y; \theta)$, and the target solution at a set of discrete collocation points (τ_i, x_i, y_i) . Specifically, the PDE residual is evaluated by substituting the predicted density into the governing diffusion equation at N_r points randomly sampled within the (τ, x, y) domain,

$$\begin{aligned} \mathcal{L}_{\text{PDE}} = & \frac{1}{N_r} \sum_{i=1}^{N_r} \left| \frac{\partial \rho_{nn}(\tau_i, x_i, y_i; \theta)}{\partial \tau} \right. \\ & + \frac{\partial [\rho_{nn}(\tau_i, x_i, y_i; \theta) v_x(\tau_i, x_i, y_i)]}{\partial x} \\ & \left. + \frac{\partial [\rho_{nn}(\tau_i, x_i, y_i; \theta) v_y(\tau_i, x_i, y_i)]}{\partial y} \right|^2 \quad (4) \end{aligned}$$

Partial derivatives with respect to the coordinates are computed via the network's automatic differentiation capability. To ensure the physical validity of the model, the predicted density $\rho_{nn}(\tau, x, y; \theta)$ is constrained by the prescribed initial and boundary conditions of the PDE. The corresponding initial condition loss \mathcal{L}_{IC} and boundary condition loss \mathcal{L}_{BC} are evaluated similarly to the PDE residual, ensuring that the neural network honors all specified physical constraints.

$$\mathcal{L}_{\text{IC}} = \frac{1}{N_{ic}} \sum_{i=1}^{N_{ic}} |\rho_{nn}(\tau_0, \mathbf{r}_{ic}^i; \theta) - \rho_0(\tau_0, \mathbf{r}_{ic}^i)|^2 \quad (5)$$

$$\mathcal{L}_{\text{BC}} = \frac{1}{N_{bc}} \sum_{i=1}^{N_{bc}} |\rho_{nn}(\tau_i, \mathbf{r}_{bc}^i; \theta) - \rho_{bc}(\tau_i, \mathbf{r}_{bc}^i)|^2 \quad (6)$$

where N_{ic} denotes the number of collocation points randomly sampled at the initial time $\tau = \tau_0$, where \mathbf{r}_{ic}^i represents the transverse coordinates (x_i, y_i) within the physical domain. The term $\rho_0(\tau_0, x, y)$ refers to the initial charm quark distribution. Similarly, N_{bc} indicates the number of temporal points τ_i sampled along the domain boundaries. These boundaries are defined by a rectangular transverse plane with vertices at $(\pm 20, \pm 20)$ fm. The residuals in Eq. (6) are evaluated by integrating across all such boundary segments.

The total loss function is a weighted sum of above terms,

$$\mathcal{L}(\theta) = \lambda_1 \mathcal{L}_{\text{PDE}} + \lambda_2 \mathcal{L}_{\text{IC}} + \lambda_3 \mathcal{L}_{\text{BC}} \quad (7)$$

where the hyperparameters λ_1 , λ_2 , and λ_3 represent the weights of the respective loss terms, ensuring training stability and convergence. To achieve a more robust optimization when modeling charm quark diffusion within

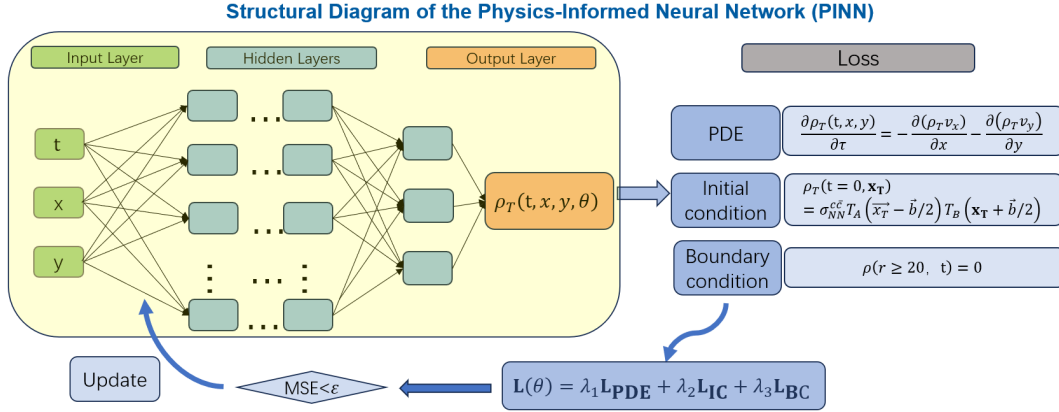


FIG. 2: Schematic architecture of the PINN utilized to resolve the charm quark density $\rho(\tau, x, y)$. The model incorporates the governing diffusion equation, initial condition and boundary conditions as physical constraints.

a fluctuating bulk medium, these hyperparameters are dynamically adjusted during iterations. Their specific values are detailed in the subsequent sections. Furthermore, during the minimization of $\mathcal{L}(\theta)$, the learning rate is varied across training iterations to enhance the accuracy of the PINN.

As illustrated in Fig. 2, the deep neural network is trained to satisfy the governing PDE while adhering to the prescribed initial and boundary conditions. The architecture consists of four fully connected hidden layers, each containing 256 neurons with Tanh activation functions. To ensure the non-negativity of the predicted density, a Softplus activation is applied to the output layer. Additionally, the velocity field required for the PDE is derived from a hydrodynamic model and pre-processed via a dedicated Velocity Field Cache module. In the training of PINN, a hybrid optimization strategy, sequential coupling of Adam and L-BFGS, have been widely adopted. Initially, the Adam optimizer, a first-order stochastic gradient-based method, is employed. Adam's adaptive learning rate allows it to rapidly escape suboptimal local minima and push the loss towards a favorable basin of attraction during the early training stages. However, due to its stochastic nature, Adam often exhibits oscillatory behavior and slow convergence near the global optimum. To refine the solution, the training transitions to L-BFGS, a second-order quasi-Newton method. L-BFGS exploits the second-order curvature information of the loss function, enabling a much faster, deterministic convergence with superior numerical precision. This transition ensures that the physical residuals (PDE constraints) are minimized to a tolerance that first-order methods typically fail to reach, thereby significantly enhancing the fidelity and accuracy of the PINN solution. The DNN parameters are updated via backpropagation by minimizing the total loss function $\mathcal{L}(\theta)$, as defined in Eq. (7).

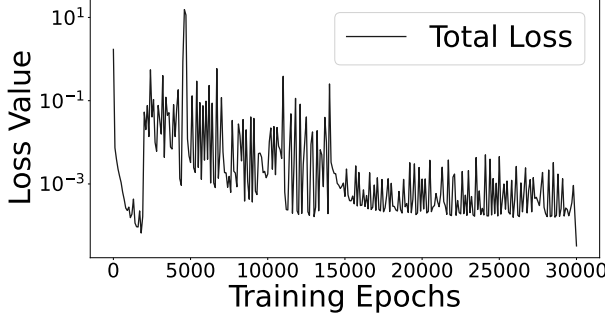
IV. NUMERICAL SOLUTIONS

The PINN training process iteratively updates the network parameters to minimize the composite loss function, ensuring that the output, $\rho_{\text{PINN}}(\tau, x, y)$, satisfies the three physical constraints simultaneously. The convergence history of this loss is presented in Fig. 3. During each training epoch, the input domain is discretized into a grid of $N_\tau \times N_x \times N_y$ points, representing the number of collocation points along the temporal and spatial directions, respectively. To enhance the network's ability to resolve the PDE dynamics, a temporal domain decomposition strategy was employed. The time interval for training is extended sequentially such as [0, 3], [0, 6], and [0, 10] fm/c (shown in the table), allowing the PINN to be trained chronologically across these stages. The specific learning rates and hyperparameters ($\lambda_1, \lambda_2, \lambda_3$) used to weight the PDE, initial condition (IC), and boundary condition (BC) constraints for each interval are summarized in Table I. The model was initially trained for 14,000 epochs using the Adam optimizer, followed by the use of the L-BFGS optimizer to further refine the solution and accelerate convergence toward a deeper local minimum. As illustrated in Fig. 3, the total loss function successfully converged to below 10^{-3} after a total of 20,000 epochs.

While a low loss function indicates that the PINN output generally satisfies the PDE and its associated initial and boundary conditions, it does not inherently guarantee local accuracy. Therefore, it is essential to evaluate the local residuals at each spatio-temporal point (τ, x, y) to determine the magnitude of deviation and verify that the model's predictions remain physically consistent across the entire domain. To establish a baseline for comparison, a fourth-order Runge-Kutta (RK4) method was employed to solve the PDE numerically. By integrating this algorithm with the prescribed initial and boundary conditions, we obtained conventional numer-

Training process				$\mathbf{L} = \lambda_1 \mathbf{L}_{\text{PDE}} + \lambda_2 \mathbf{L}_{\text{IC}} + \lambda_3 \mathbf{L}_{\text{BC}}$		
IC Pretrain						
Epochs		Learning Rate		Optimizer	λ_1	λ_2
2000		1e-3		Adam	0.0	1.0
PDE Curriculum Learning						
Stage	Time range of data	Epochs	Learning Rate	Optimizer	1.0	10.0
1	0~3.0	5000	1e-3	Adam		
2	0~6.0	7000	5e-4	Adam		
3	0~10.0	14000	1e-4	Adam		2.0
L-BFGS Finetune						
Learning Rate			Optimizer		5.0	5.0
0.8			L-BFGS			

TABLE I: Training process parameters and loss weights across different stages.

FIG. 3: The total loss function $\mathcal{L}(\theta)$ of the PINNs varying with the number of training epochs.

ical solutions to validate the accuracy and performance of the PINN framework. In Fig. 4, the transverse spatial distribution, $\rho_T(\tau, x, y)$, of the charm quark density in the hydrodynamic medium of 5.02 TeV Pb-Pb collisions (with an impact parameter $b = 6.0$ fm) is presented. The results from the traditional numerical method (RK4) and the PINN are plotted in the upper and lower panels, respectively, with color gradients representing the magnitude of the density. As illustrated, the charm quark distribution generated by the PINN is stable, devoid of unphysical fluctuations, and visually indistinguishable from the RK4 results. For a more rigorous quantitative comparison, Fig. 5 displays the results for the charm quark density restricted to the $y = 0$ plane, denoted as $\rho_T(\tau, x, y = 0)$. In this figure, the RK4 results are represented by discrete points, while the PINN predictions are shown as solid lines. The nearly perfect overlap between the data points and the lines demonstrates that the PINN model accurately captures the charm quark diffusion process across all spatio-temporal coordinates.

This excellent agreement with the conventional numerical baseline further validates the model's reliability.

Since the total number of heavy quarks is conserved within the diffusion equation, one can verify the model's physical consistency by checking whether the PINN output adheres to this constraint. Utilizing the charm quark density $\rho_{\text{PINN}}(\tau, x, y)$ predicted by the PINN, the total charm quark abundance at each time step, $N_c(\tau)$, is calculated and presented in Fig. 6. Across different time intervals, the total quark number remains approximately conserved, exhibiting only negligible deviations. These minor discrepancies are attributed to the inherent numerical approximation errors of the PINN during the optimization process.

Once properly trained, the PINN framework can efficiently simulate charm quark diffusion in fluctuating media, where velocity fields vary significantly compared to smooth, idealized cases. This capability substantially accelerates the computation of charm densities required for modeling charmonium regeneration. In future work, we intend to extend the PINN framework to solve the Fokker-Planck equation, enabling the simultaneous modeling of charm quark diffusion in both spatial and momentum space.

V. SUMMARY

In this work, we employ Physics-Informed Neural Networks (PINNs) to solve the partial differential equations (PDEs) governing charm quark diffusion within the expanding hot QCD medium generated in relativistic heavy-ion collisions. Given their large mass, charm quarks are primarily produced during initial hard parton scatterings; consequently, their total number is conserved as they propagate through the deconfined medium. The

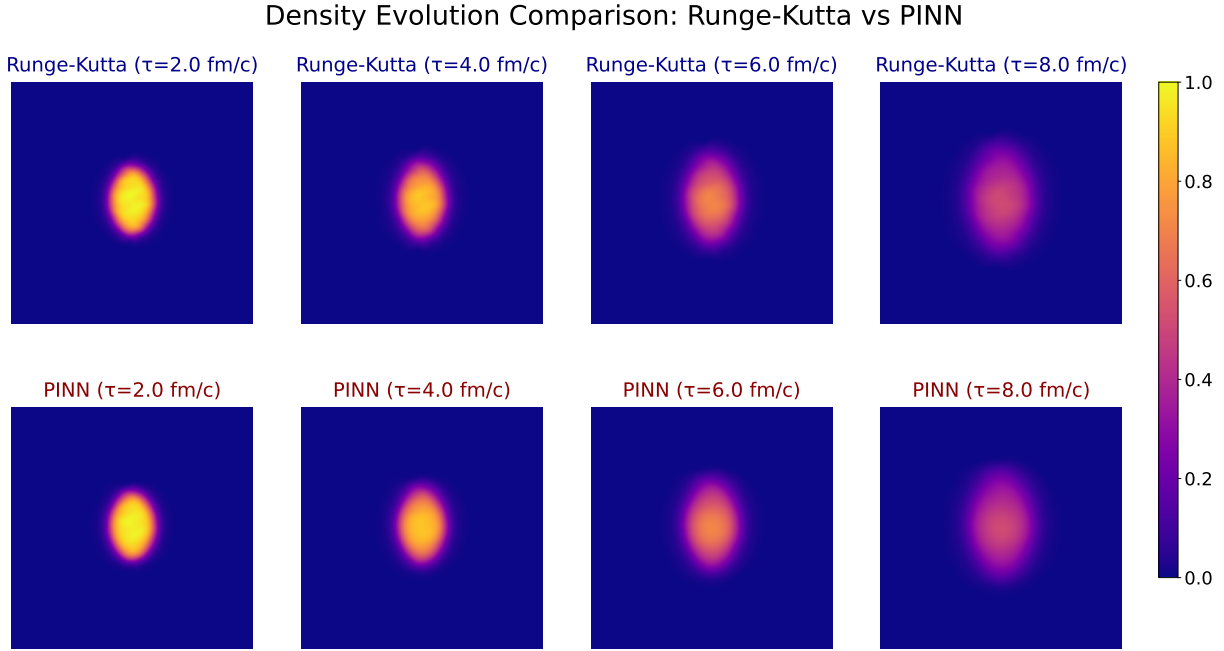


FIG. 4: Charm quark density $\rho_T(\tau, x, y)$ at mid-rapidity in 5.02 TeV Pb-Pb collisions with an impact parameter $b = 6.0$ fm. The upper and lower panels display the results obtained from the fourth-order Runge-Kutta (RK4) method and the PINN framework, respectively. The color scale indicates the local density magnitude.

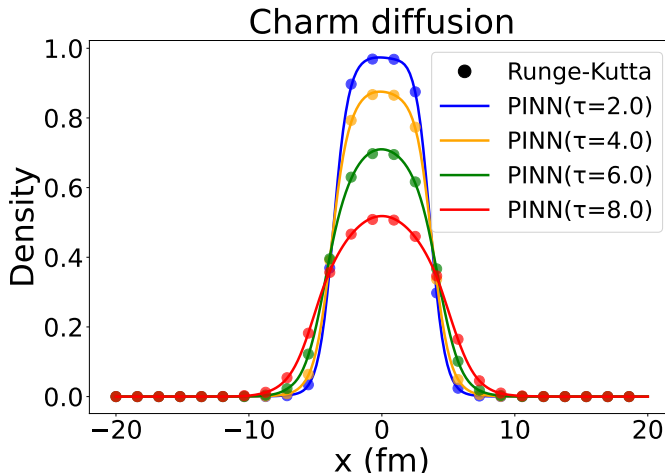


FIG. 5: Temporal evolution of the charm quark spatial density $\rho_T(\tau, x, y = 0)$ at mid-rapidity in 5.02 TeV Pb-Pb collisions with an impact parameter $b = 6.0$ fm. Numerical solutions obtained via the fourth-order Runge-Kutta (RK4) method are represented by discrete points, while the PINN predictions are shown as solid lines.

diffusion dynamics are dictated by the underlying fluid velocity fields, which evolve spatio-temporally according to hydrodynamic models. By encoding these complex velocity fields directly into the PDE and incorporating

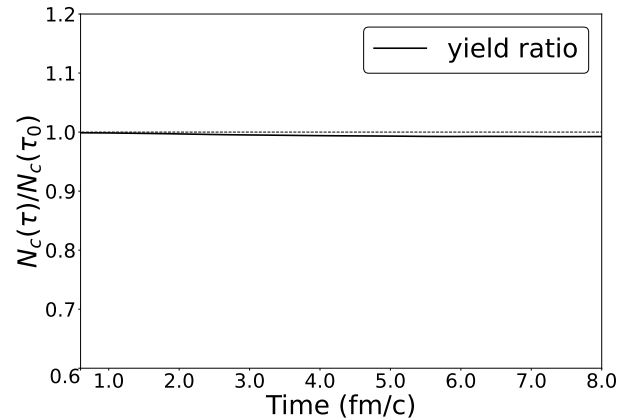


FIG. 6: Temporal evolution of the normalized charm quark abundance, $N_c(\tau)/N_c(\tau_0)$, at mid-rapidity in 5.02 TeV Pb-Pb collisions with an impact parameter $b = 6.0$ fm. The total number N_c is obtained by integrating the density $\rho_{\text{PINN}}(\tau, x, y)$ predicted by the PINN model.

specific initial and boundary conditions, the PINN model accurately characterizes charm quark transport. Our results demonstrate that the PINN predictions align closely with those obtained from traditional numerical schemes, such as the fourth-order Runge-Kutta method. Furthermore, this framework enables the rapid and precise calculation of event-by-event charm quark densities under varying velocity fields, providing a robust computational

tool for studying charmonium regeneration in fluctuating media.

Acknowledgement: This work is supported by the National Natural Science Foundation of China (NSFC) under Grant Nos. 12575149 and 12175165.

[1] A. Bazavov *et al.*, *Phys. Rev. D* **85**, 054503 (2012), arXiv:1111.1710 [hep-lat].

[2] S. S. Adler *et al.* (PHENIX), *Phys. Rev. C* **69**, 034909 (2004), arXiv:nucl-ex/0307022.

[3] K. Aamodt *et al.* (ALICE), *Phys. Rev. Lett.* **105**, 252302 (2010), arXiv:1011.3914 [nucl-ex].

[4] L. Pang, Q. Wang, and X.-N. Wang, *Phys. Rev. C* **86**, 024911 (2012), arXiv:1205.5019 [nucl-th].

[5] C. Gale, S. Jeon, and B. Schenke, *Int. J. Mod. Phys. A* **28**, 1340011 (2013), arXiv:1301.5893 [nucl-th].

[6] U. Heinz and R. Snellings, *Ann. Rev. Nucl. Part. Sci.* **63**, 123 (2013), arXiv:1301.2826 [nucl-th].

[7] T. Matsui and H. Satz, *Phys. Lett. B* **178**, 416 (1986).

[8] M. He, R. J. Fries, and R. Rapp, *Phys. Rev. Lett.* **110**, 112301 (2013), arXiv:1204.4442 [nucl-th].

[9] Y. Liu, B. Chen, N. Xu, and P. Zhuang, *Phys. Lett. B* **697**, 32 (2011), arXiv:1009.2585 [nucl-th].

[10] S. Cao, G.-Y. Qin, and S. A. Bass, *Phys. Rev. C* **92**, 024907 (2015), arXiv:1505.01413 [nucl-th].

[11] B. Chen, L. Jiang, X.-H. Liu, Y. Liu, and J. Zhao, *Phys. Rev. C* **105**, 054901 (2022), arXiv:2107.00969 [hep-ph].

[12] W.-J. Xing, S.-Q. Li, S. Cao, and G.-Y. Qin, *Phys. Rev. C* **110**, 024903 (2024), arXiv:2404.12601 [hep-ph].

[13] R. L. Thews, M. Schroedter, and J. Rafelski, *Phys. Rev. C* **63**, 054905 (2001), arXiv:hep-ph/0007323.

[14] V. Greco, C. M. Ko, and R. Rapp, *Phys. Lett. B* **595**, 202 (2004), arXiv:nucl-th/0312100.

[15] A. Andronic, P. Braun-Munzinger, K. Redlich, and J. Stachel, *Phys. Lett. B* **571**, 36 (2003), arXiv:nucl-th/0303036.

[16] L. Yan, P. Zhuang, and N. Xu, *Phys. Rev. Lett.* **97**, 232301 (2006), arXiv:nucl-th/0608010.

[17] K. Zhou, N. Xu, Z. Xu, and P. Zhuang, *Phys. Rev. C* **89**, 054911 (2014), arXiv:1401.5845 [nucl-th].

[18] C. Pan, S. Zheng, M. Yang, Z. Liu, and B. Chen, *Phys. Rev. C* **108**, 034903 (2023), arXiv:2303.12262 [nucl-th].

[19] M. Singh, M. Kurian, S. Jeon, and C. Gale, *Phys. Rev. C* **108**, 054901 (2023), arXiv:2306.09514 [nucl-th].

[20] M. Raissi, P. Perdikaris, and G. E. Karniadakis, *Journal of Computational Physics* **378**, 686 (2019).

[21] A. Farea, O. Yli-Harja, and F. Emmert-Streib, *AI* **5**, 1534 (2024).

[22] S. Wang, X. Yu, and P. Perdikaris, *Journal of Computational Physics* **449**, 110768 (2022), arXiv:2007.14527.

[23] D. Zhang, L. Guo, and G. E. Karniadakis, *SIAM J. Sci. Comput.* **42**, A639 (2020), arXiv:1905.01205 [cs.LG].

[24] L. Yang, D. Zhang, and G. E. Karniadakis, *SIAM J. Sci. Comput.* **42**, A292 (2020), arXiv:1811.02033 [cs.LG].

[25] A. Sedykh, M. Podapaka, A. Saginalieva, K. Pinto, M. Pflitsch, and A. Melnikov, *Mach. Learn. Sci. Tech.* **5**, 025045 (2024), arXiv:2304.11247 [cs.LG].

[26] S. Cai, Z. Mao, Z. Wang, M. Yin, and G. E. Karniadakis, *Acta Mechanica Sinica* **37**, 1727–1738 (2021).

[27] A. D. Jagtap and G. E. Karniadakis, *Commun. Comput. Phys.* **28**, 2002 (2020).

[28] H. Song, Y. Zhou, and K. Gajdosova, *Nucl. Sci. Tech.* **28**, 99 (2017), arXiv:1703.00670 [nucl-th].

[29] J. Zhao, B. Chen, and P. Zhuang, *Phys. Rev. C* **105**, 034902 (2022), arXiv:2112.00293 [hep-ph].

[30] H. Song and U. W. Heinz, *Phys. Rev. C* **77**, 064901 (2008), arXiv:0712.3715 [nucl-th].

[31] B. Schenke, S. Jeon, and C. Gale, *Phys. Rev. C* **82**, 014903 (2010), arXiv:1004.1408 [hep-ph].

[32] B. Schenke, S. Jeon, and C. Gale, *Phys. Rev. Lett.* **106**, 042301 (2011), arXiv:1009.3244 [hep-ph].

[33] A. Bazavov *et al.* (HotQCD), *Phys. Rev. D* **90**, 094503 (2014), arXiv:1407.6387 [hep-lat].

[34] J. E. Bernhard, J. S. Moreland, S. A. Bass, J. Liu, and U. Heinz, *Phys. Rev. C* **94**, 024907 (2016), arXiv:1605.03954 [nucl-th].

[35] D. Banerjee, S. Datta, R. Gavai, and P. Majumdar, *Phys. Rev. D* **85**, 014510 (2012), arXiv:1109.5738 [hep-lat].

[36] A. Francis, O. Kaczmarek, M. Laine, T. Neuhaus, and H. Ohno, *Phys. Rev. D* **92**, 116003 (2015), arXiv:1508.04543 [hep-lat].

[37] J. Zhao and B. Chen, *Phys. Lett. B* **776**, 17 (2018), arXiv:1705.04558 [nucl-th].